J. Cent. South Univ. (2021) 25: −
DOI:

Springer

Compatibility research of laser additive repairing (LAR) TA15 forgings with Ti6Al4V-*x*TA15 alloy

Jun Yu(于君)[1,2], Yepan Song(宋业盼)[1,2], Xin Lin(林鑫)[1,2], Zhenjie Cao(曹镇杰)[1], Quanren Zeng(曾泉人)[3,4], Junjie Wang (王俊杰)[1], Weidong Huang(黄卫东) [1,2]

1. State Key Laboratory of Solidification Processing, Northwestern Polytechnical University, Xi'an, Shaanxi, 710072, PR China
2. Key Laboratory of Metal High Performance Additive Manufacturing and Innovative Design, MIIT China, Northwestern Polytechnical University, Xi'an, Shaanxi 710072, PR China
3. Advanced Forming Research Centre, National Manufacturing Institute Scotland, 85 Inchinnan Drive, Renfrewshire PA4 9LJ, UK
4. Department of Design, Manufacture and Engineering Management (DMEM), University of Strathclyde, 75 Montrose Street Glasgow, G1 1XJ, UK1

Abstract: The application of mixed powders in a different mass fraction on LAR can be an effective way to guarantee the performance and functionality of repaired part in time. A convenient and feasible approach is presented to repair TA15 forgings by employing Ti6Al4V-*x*TA15 mixed powders in this paper. The performance compatibility of Ti6Al4V-*x*TA15 powders from the aspects of microhardness, tensile property, heat compacity, thermal expansion coefficient and corrosion resistance with the TA15 forgings are fully investigated. The primary α laths are refined and the volume fraction of the secondary α phase is increased by increasing the mass fraction of TA15 in the mixed Ti6Al4V-*x*TA15 powders, leading to varied performances. In conclusion, the mixed powders Ti6Al4-70%TA15 (*x*=70%) is the most suitable candidate and is recommended as the raw material for LAR of TA15 forgings based on an overall consideration of the compatibility calculations of the laser repaired zone with the wrought substrate zone.

Key words: TA15 alloy; Ti6Al4V alloy; laser additive repairing; compatibility

Cite this article as: YU Jun, SONG Ye-pan, LIN Xin, CAO Zhen-jie, ZENG Quan-ren, WANG Jun-jie, HUANG Wei-dong. Compatibility research of laser additive repairing (LAR) TA15 forgings with Ti6Al4V-*x*TA15 alloy [J]. Journal of Central South University, 2021, 27(10): . DOI:

1 Introduction

The laser additive repairing (LAR) technique can be adapted to directly repair the damaged zone for a three-dimensional (3D) component with complex geometry due to its advantages in generating small heat-affected zone and deformation with low stress. The non-defect metallurgical bonding within the repaired part performs good or even better mechanical properties than that of the original, as well as a superior dimensional accuracy. The studies of the researchers CHAMANFAR [1], GRIFFITH [2],

Received date: 0000−00−00; **Accepted date:** 0000−00−00
Corresponding author: Jun Yu, PhD, Associate Professor; Tel: +86-19991909896; E-mail: yujun@nwpu.edu.cn; ORCID: 0000-0002-9142-0929
Xin Lin, PhD, Professor; Tel: +86-29-88494001; E-mail: xlin@nwpu.edu.cn; ORCID: 0000-0002-7491-8928

FATOBA [3], FACCHINI [4], and FADIDA [5] et al. have proved that finer and more uniform microstructure are readily generated by laser additive manufacturing (LAM) due to its instantaneous solidification process, leading to a higher strength but reduced plasticity compared to the forged counterpart. In this case, some problems could occur if LAR is restricted to progress between the same material as ZHAO and MARAZANI [6-8] mentioned. SUN et al. [9] studied the effect of different scanning modes on the microstructure to improve the mechanical properties, while CHEN et al. [10] had focused on ductility enhancement. Therefore, the compatibility between the laser repaired zone (LRZ) and the remaining original is required to take into account seriously, to improve their compatibility in performance.

Nowadays, titanium alloys are widely used for fabricating lightweight and high-end structural components in the field of aerospace and national defense. Among them, TA15 and Ti6Al4V are typical near-α and α+β titanium alloys with wide applications both at room or at high temperature. Actually, in ZHOU's study the tensile strength of LAM TA15 is similar to that of TA15 forgings, but its plasticity is close to the lower limit of the forging standard [11]. Furthermore, it has been reported by LI [12] and XU [13], the plasticity of LAM TA15 can be increased obviously if a certain amount of Ti6Al4V powders was added, only accompanied by a slightly lowered strength.

Therefore, more attention should be paid to the performance difference between the laser repaired zone (LRZ) and the original base material for the high-quality reparation of titanium alloy. In principle, the compatibilities of Ti6Al4V-*x*TA15 alloys with TA15 and Ti6Al4V forgings need to be investigated, respectively. The compatibility of Ti6Al4V-*x*TA15 alloys with TA15 forgings during LAR is studied in the present work by comparing the microstructure and mechanical properties of Ti6Al4V-*x*TA15 LRZ with those of the forged TA15 parts. In addition, the physical and chemical performances of LRZ of Ti6Al4V-*x*TA15 were investigated in detail to clarify the influence of solute elements, such as Fe, Al, Mo, Zr and V, on the thermal expansion coefficient, specific heat capacity and corrosion resistance of titanium alloy.

2 Experimental Setup

2.1 Powders preparation

The powders employed were TA15 and Ti6Al4V spherical powders which were prepared by the plasma rotating electrode method with a size range of 45~180μm. The morphologies of the two types of powders are shown in Figure 1. We can see that the Ti6Al4V powders include a large portion of small particles while TA15 powders are more uniform in their particle size distribution. The particle size difference between Ti6Al4V and TA15 may lead to composition fluctuation in the laser additively repaired zone. The compositions of the two types of powders are shown in Table 1. The Mo equivalents are calculated as 2.698 for Ti6Al4V and 3.322 for TA15 in terms of Eq. (1) [14] respectively. Therefore, the β stabilizer is strengthened with the increase of the TA15 mass fraction, leading to the increase in Mo element content.

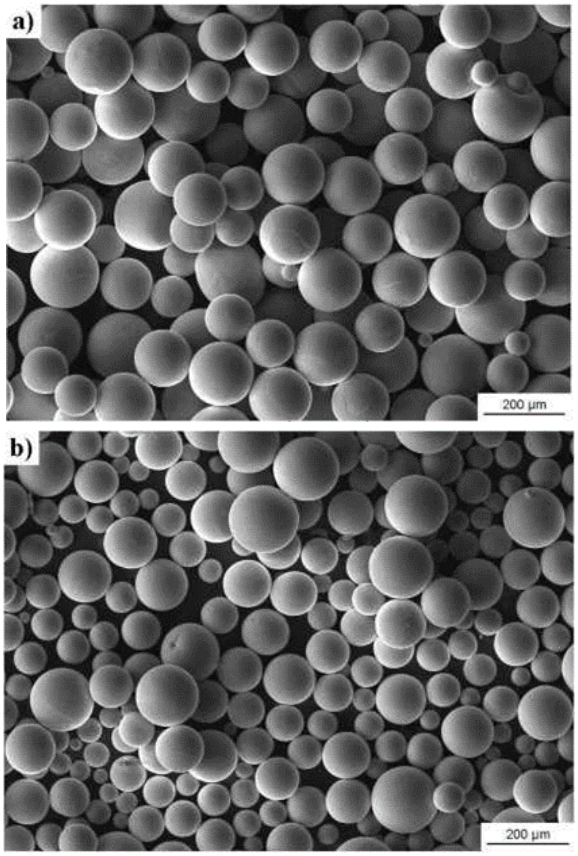

Figure 1 Morphologies of powders used in the present work: (a) TA15 and (b) Ti6Al4V.

$$[Mo]_{eq} = Mo + \frac{Nb}{3.3} + \frac{Ta}{4} + \frac{W}{2} + \frac{Cr}{0.6} + \frac{Mn}{0.6} + \frac{V}{1.5} + \frac{Fe}{0.5} + \frac{Co}{0.9} + \frac{Ni}{0.8} \quad (1)$$

Table 1 Chemical compositions of TA15 and Ti6Al4V powders (wt.%)

Alloy	TA15	Ti6Al4V
Al	6.65	6.78
V	2.23	4.01
Mo	1.79	-
Zr	2.12	-
Fe	0.09	0.05
N	0.008	0.01
C	0.006	0.022
H	0.024	0.018
O	0.13	0.14
Si	<0.04	<0.04
Ti	Bal.	Bal.

For the mixed Ti6Al4V-*x*TA15 powders, the TA15 powders' mass fraction of 50%, 60%, 70%, 80%, 90%, and 100% were selected for the LAR trials. Figure 2 is the calculated elemental content in terms of the specified weight percentage of TA15 powder in the mixed powders. As the weight percentage of TA15 powder increases, the element content of α stabilizer, Al, decreases very slightly; meanwhile, the element content of β stabilizer, Mo, increases apparently. In addition, the ratio of a neutral element, Zr, also increases correspondingly.

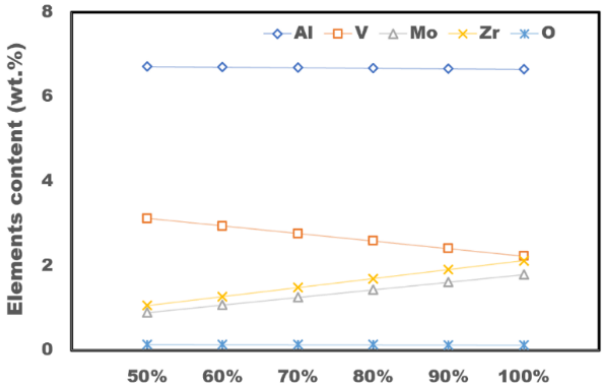

Figure 2 Chemical compositions of the Ti6Al4V-*x*TA15 alloy in wt.%

2.1 Powders preparation

A system consisted of LDF 6000-60 semiconductor laser, a five-axis NC worktable, DPSF-2 high precision adjustable powder feeder, coaxial powder feeding nozzle, inert atmosphere protection chamber was used for the LAR experiment. To prevent the LRZ from severe oxidation, argon was employed both as the shielding gas and carrier gas. The powders were dried firstly and then blended through a 2-hour ball-milling process. The annealed TA15 forging plates were used as wrought substrate zone (WSZ) and their surfaces were polished and cleaned with acetone before LAR trials. Table 2 shows the processing parameters of LAR Ti6Al4V-*x*TA15. The scanning directions are perpendicular to each other between adjacent layers during the LAR process.

The microstructure on the cross-section perpendicular to the laser scanning direction was analyzed by optical microscope (OM) and scanning electron microscope (SEM). The Kroll reagent with a volume ratio of HF: HNO3: H2O = 1: 3: 50 was used as the etchant. The LAR blocks with the mixed Ti6Al4V-*x*TA15 powders shown in Figure 3(a). Three kinds of tensile testing specimens, which cover a full laser repaired zone (LRZ, shown as Figure 3 (b1)), a full wrought substrate zone (WSZ, shown as Figure 3 (b3)) and half LRZ + half WSZ (shown as Figure 3 (b2)), were prepared in three pieces per kind. The hardness of the samples was measured every 0.5 mm from the WSZ to the upper of LRZ.

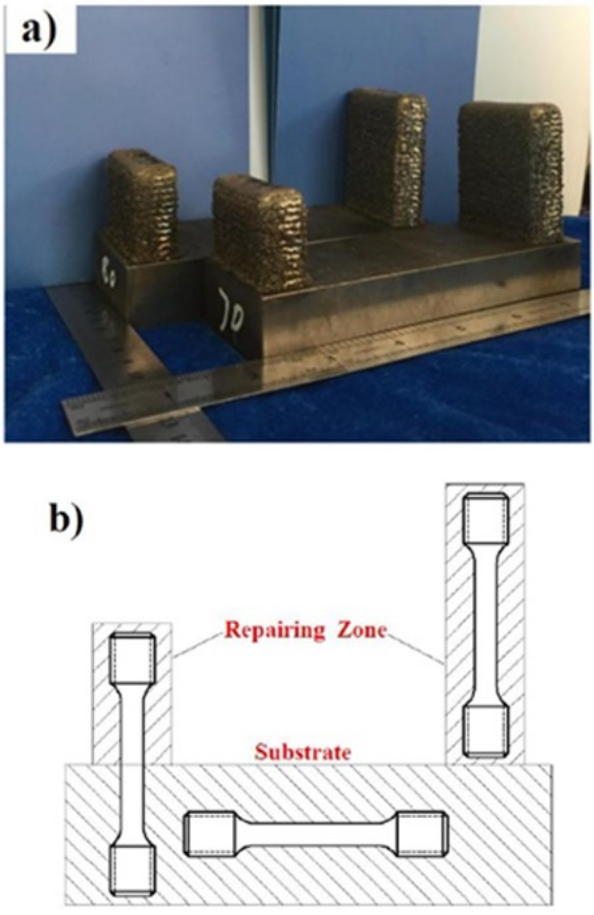

Figure 3 LAR blocks for tensile testing (a) deposited

sample blocks (b) sampling sketch map where b1) testing sample of repairing zone (LRZ); b2) testing sample of LRZ+WSZ; b3) testing sample of wrought substrate zone (WSZ).

Table 2 Processing parameters of LAR trial/experiment with Ti6Al4V-*x*TA15 powders

Laser power /W	Scanning speed /mm·min^{-1}	Laser Spot-diameter /mm	Powder feeding rate /g·min^{-1}	Layer thickness /mm
1800	900	5	11	0.6

2.3 Thermo-physical parameters measurement and electrochemical test

The thermal expansion coefficient was tested by the DIL402C instrument from the NETZSCH company. Before testing, cylindrical samples were machined to the size of the standard sample, i.e., 6 mm×25mm. The oxidation film on the surface was polished off with sandpaper and both ends were polished parallel to the laser scanning direction. The baseline of the standard sample was measured before the test; the heating range was between 303K to 873K and the heating rate adopted is 10 K/min.

The furnace was vacuumed to remove oxygen before testing and the chlorine gas was continuously filled into the furnace with a flow rate of 50 ml/min during the test. The variation of linear expansion coefficient with temperature was calculated based on the Eqs. (2) and (3). Equation (2) was used to calculate the average linear expansion coefficient $\bar{\alpha}$ and equation (3) was used to calculate the instantaneous linear expansion coefficient α_{T_i}.

$$\bar{\alpha} = \Delta L/(L_0 \cdot \Delta T) \quad (2)$$

$$\alpha_{T_i} = \lim_{T_2 \to T_1} (L_2 - L_1)/((T_2 - T_1) \cdot L_0) \quad (3)$$

in which, the L0, ΔL and ΔT in both equations represent the initial length, the elongation and the change of temperature respectively.

The specific heat capacity was measured by the STA449C synchronous thermal analyzer produced by Netzsch Company. The LRZ was processed into wafers of 5mm×1.2mm and their oxidation film was polished off with sandpaper (from 240 mesh to 2000 mesh,). The mass of each specimen was close to the sapphire standard sample (85.00 mg). Platinum rhodium crucible (with lining) was used in the experiment. The temperature range was 303K - 873K with a heating rate of 10 K/min and the isothermal measurements were performed at 303K and 873K for 15 minutes, respectively. The baseline of an empty crucible was measured twice before the test and the differential scanning calorimetry (DSC) curve of the sapphire standard sample was measured as the stable baseline reached. Finally, the curves of specific heat capacity Cp with temperature were illustrated based on the DSC curve of the sample as shown in Figure 4. The value of specific heat capacity Cp of the sample was calculated in terms of Eqs. (4) and (5).

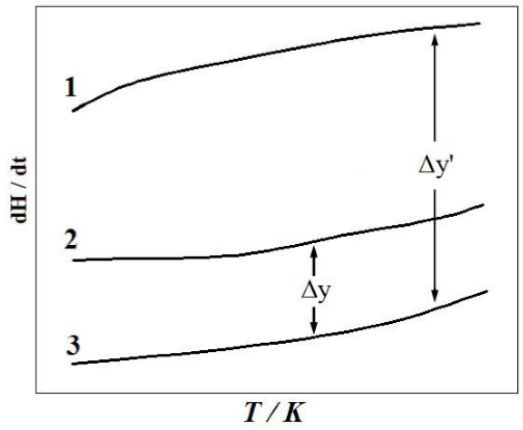

Figure 4 DSC curves to measure specific heat capacity: 1-Standard 2-Sample 3-Baseline

$$\Delta y/\Delta y' = (DSC_{sample} - DSC_{bas})/(DSC_{standard} - DSC_{bas}) = Cp_{sample} \times m_{sample}/Cp_{standard} \times m_{standard} \quad (4)$$

$$Cp_{sample} = \Delta y/\Delta y' \times m_{standard}/m_{sample} \times Cp_{standard} \quad (5)$$

The LRZ was processed into a circular sample by wire electrical discharge machining (EDM) and both sides of the wafer were parallel to the laser scanning direction. The size was the same as that of the standard sample in the fixture (Φ15 mm×5 mm). The tested surface was firstly polished by 240#, 600#, 1000#, 1500# and 2000# water grinding sandpaper until no scratches visible; then the polished surface was washed with deionized water and cleaned with acetone. The 500 mL of 3.5% NaCl solution was added into the electrolytic cell and the three electrodes were accurately connected to the three wires of an electrochemical workstation. The

sample was immersed in NaCl solution for 12 hrs. When measuring the Tafel curve, the basic parameters of the experiment were set as the potential ranging from -1 V to 1.5 V in a scanning rate of 0.001 V/S. The corrosion resistance was tested by CHI660B electrochemical workstation. The potentiodynamic polarization curve was measured by a three-electrode system, in which the platinum plate and the saturated KCl calomel electrode (SCE) were used as an auxiliary electrode and reference electrode respectively.

3 Results and discussions

3.1 Composition and microstructure of LAR Ti6Al4V-*x*TA15

There is a difference in particle size distribution (PSD) between the TA15 and Ti6Al4V powders which was shown in Figure 1. According to the reference report, powder travel speed closely depends on the density and particle size; it decreases as the density decreases or as the particle size increases for the LAM process [15,16]. To avoid the heterogeneity of components in the LRZ caused by stratification of different powders during the powders feeding process, it is necessary to confirm the composition homogeneity of LRZ. Table 3 shows the composition of alloy elements within the LRZ measured by electron diffraction spectrum (EDS) at different mass fraction of TA15 (*i.e.* *x*=50%, 60%, 70%, 80%, 90% and 100%). The average value was calculated from 20 randomly-selected points to measure the composition/mass fraction of each element in the LRZ. Basically, there was an acceptable deviation from the calculated contents in the LRZ contributed by their similar densities of 4.45 g/cm3 for TA15 and 4.44g/cm3 for Ti6Al4V.

Table 3 Chemical compositions of the Ti6Al4V-*x*TA15alloy in LRZ (wt.%)

Alloy	50%	60%	70%	80%	90%	100%
Al	6.715	6.702	6.689	6.676	6.663	6.65
V	3.12	2.942	2.764	2.586	2.408	2.23
Mo	0.895	1.074	1.253	1.432	1.611	1.79
Zr	1.06	1.272	1.484	1.696	1.908	2.12
O	0.135	0.134	0.133	0.132	0.131	0.13
Ti	Bal.	Bal.	Bal.	Bal.	Bal.	Bal.

Figure 5 shows the macro- and micro- structure morphology of Ti6Al4V-*x*TA15 alloy with different powder mass fraction, *x*, on the annealed TA15 WSZ. The macrostructure is composed of β columnar (0.4 ~ 0.8 mm in width) in the form of epitaxial growth along the deposition direction. Besides, the columnar to equiaxed transition (CET) occurred at the top with a height of 800~1000 μm. A good metallurgical bonding was produced based on observation on the remelted zone (RZ) in a depth of 700 ~ 900 μm. Besides, the primary β columnar is slenderer or refined with the ratio *x* raised because of the increment of the quantity of high melting point elements Mo and Zr. And the heat-affected zone (HAZ) of the dark strip area within the WSZ is presented clearly, leading by the difference microstructure that is revealed in the illustrations. The microstructure of Ti6Al4V-*x*TA15 specimens mainly consisted of basketweave-like primary α laths and retained the β phase. The α laths were refined with more TA15 quantity. Detailly, the average length of α lath of 50%TA15 is concentrated between 15-20 μm and the average width is about 1.04 μm, as shown in Figure 5 (a). Then the average length of α lath varies to 50μm at most and meanwhile, the average width is lowered to about 0.42 μm. With the increase of TA15 mass fraction, the content of the most effective β stabilizer Mo is increased, which inhibits the growth of the α phase.

Figure 5 (e) is the transition of microstructure from the LRZ to the WSZ in a sequence of upper LRZ, LRZ, HAZ and WSZ from top to the bottom illustrated as Figure 6 (a), (b), (c) and (d), respectively. It can be seen that the α lath at the bottom of WSZ is relatively coarse in Figure 6 (d). Part of the α laths is further roughened, accompanied by a small amount of secondary α phase precipitated due to the effect of multiple heating and heat accumulation at HAZ as shown in Figure 6 (c). The difference of corrosion resistance to the Kroll reagent between the primary α phase and secondary α phase in abundance lead to the dark stripe phenomenon appeared under OM. The micro-structure is refined because of the high cooling rate in the LRZ of Figure 6 (b), revealing a relatively disordered α+β basketweave morphology. In comparison, the α laths were slimmed in Figure 6 (a) without the cycled heating effect in the upper LRZ.

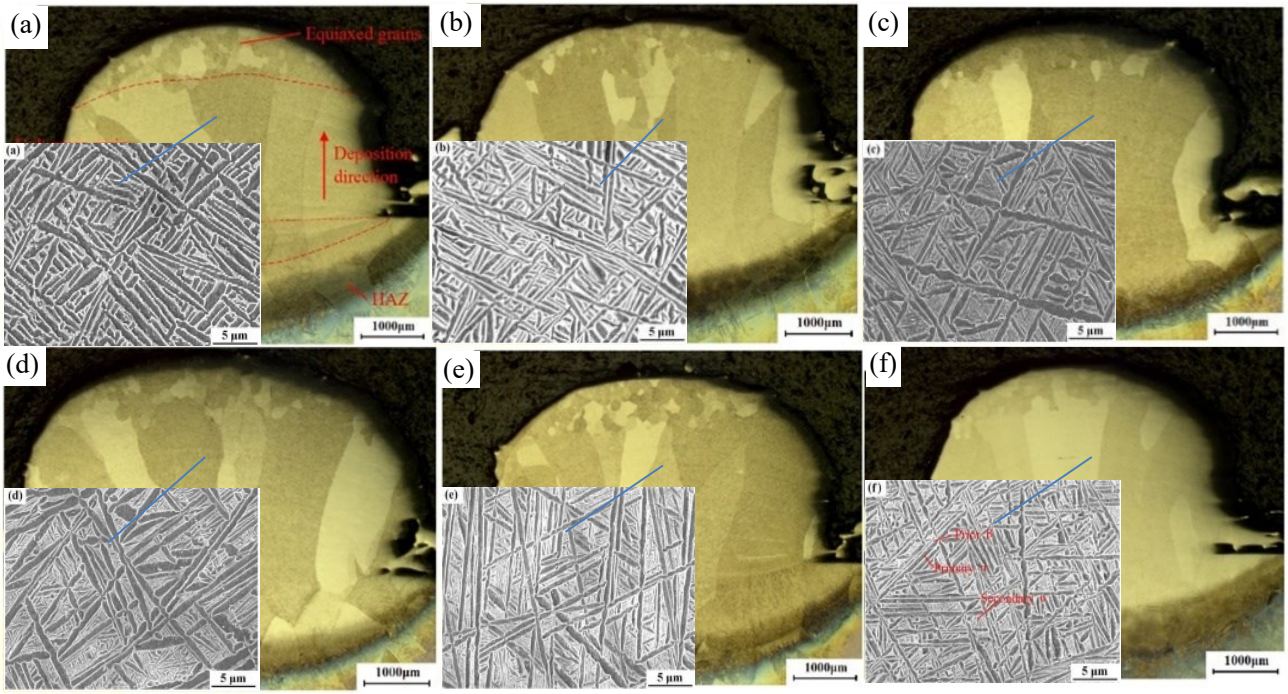

Figure 5 Macrostructure and microstructure of the Ti6Al4V-*x*TA15 alloy (a) 50%TA15 (b) 60%TA15 (c) 70%TA15 (d) 80%TA15 (e) 90%TA15 (f) 100%TA1

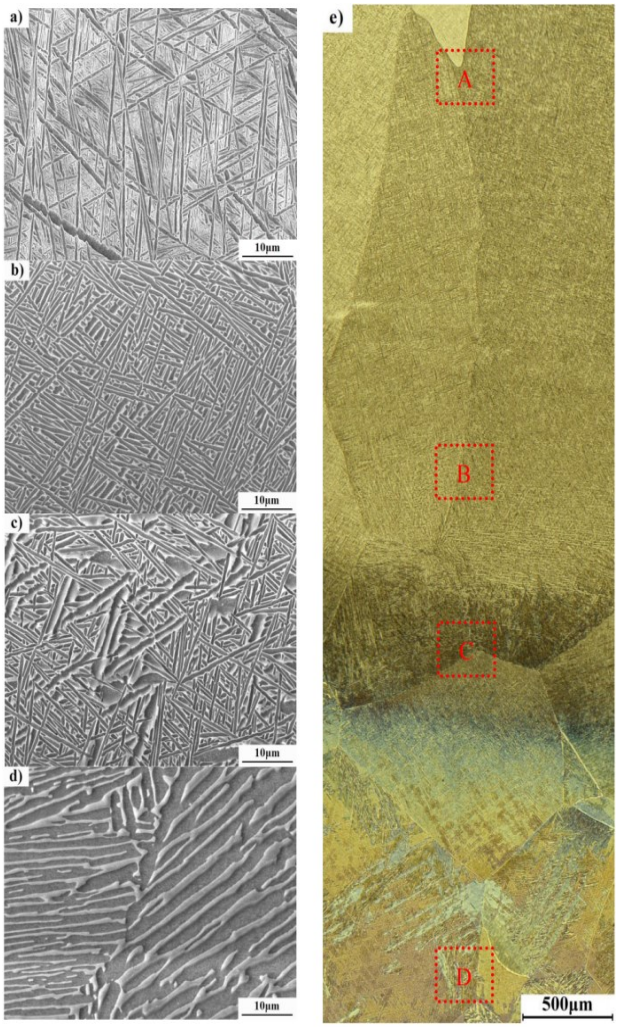

Figure 6 Transition of microstructure from LRZ to WSZ (at 70% TA15) (a) upper LRZ (b) LRZ (c) HAZ (d) WSZ (e) whole view

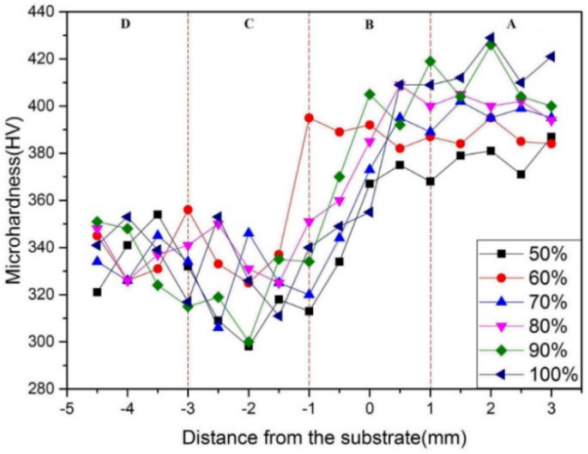

Figure 7 Hardness of the Ti6Al4V-*x*TA15 alloy from the WSZ to the LRZ

3.2 Mechanical properties of Ti6Al4V-*x*TA15

A thin-walled specimen was subject to a hardness test with a height of 3 mm and the WSZ is 5 mm. The hardness test points were taken every 0.5 mm from the bottom of the WSZ to LRZ. Figure 7 shows the measured hardness curve. The zones A, B, C, and D represent the top of the LRZ, the interfacial zone, the HAZ and the bottom of WSZ, respectively. The microhardness of zone A, B, C and D in Figure 7 corresponds to the microstructure of (a), (b), (c) and (d) in Figure 6, respectively. Generally, the hardness increases from the WSZ to LRZ because of the thinning of α laths formed in the LRZ. And the data from LRZ are more stable varied in the

amplitude of around 20HV for a certain powder, compared to a 40HV or so for the WSZ in Figure 7. In addition, the hardness for Ti6Al4V-*x*TA15 goes higher with the increase of TA15 mass fraction *x*, which is mainly caused by the effect of microstructure refinement as shown in Figure 6.

Figure 8 shows the tensile properties of the LRZ with Ti6Al4V-*x*TA15 mixed powders along with the deposition height at room temperature. It shows that the tensile strength of LRZ is higher than that of the annealed TA15 forgings. With the increase of TA15 mass fraction (*i.e. x*) in the mixed Ti6Al4V-*x*TA15 powders, the tensile strength of LRZ increases continuously. The tensile strength of the LAR sample with Ti6Al4V-50%TA15 is the lowest; it is 1042 MPa and only 10.4% higher than that of the annealed TA15 forgings which is 944 MPa. The ultimate tensile strength of the LAR sample with 100% TA15 (*i.e.* Ti6Al4V-100%TA15) reaches 1102.97 MPa. Meanwhile, the elongation (ε) shows a slightly decreasing tendency as the mass fraction of TA15 in the mixed powders increases. The reduction of area (ψ) is sensitive to the powder ratio, leading to a maximal decrement at the 100% TA15 LRZ compared to the TA15 WSZ. The performance on strength and plasticity is closely related to the macro- and microstructure morphology.

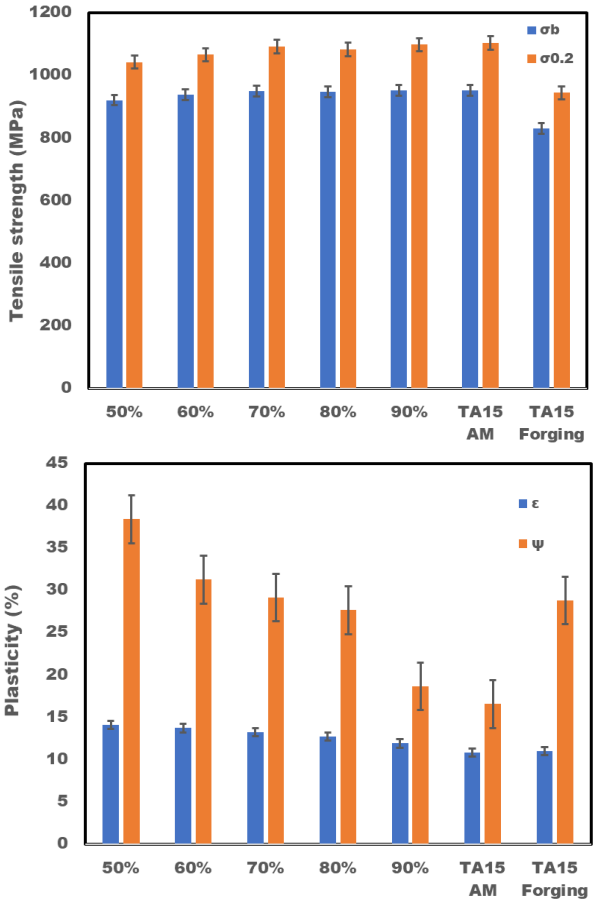

Figure 8 Tensile property of the Ti6Al4V-*x*TA15 alloy

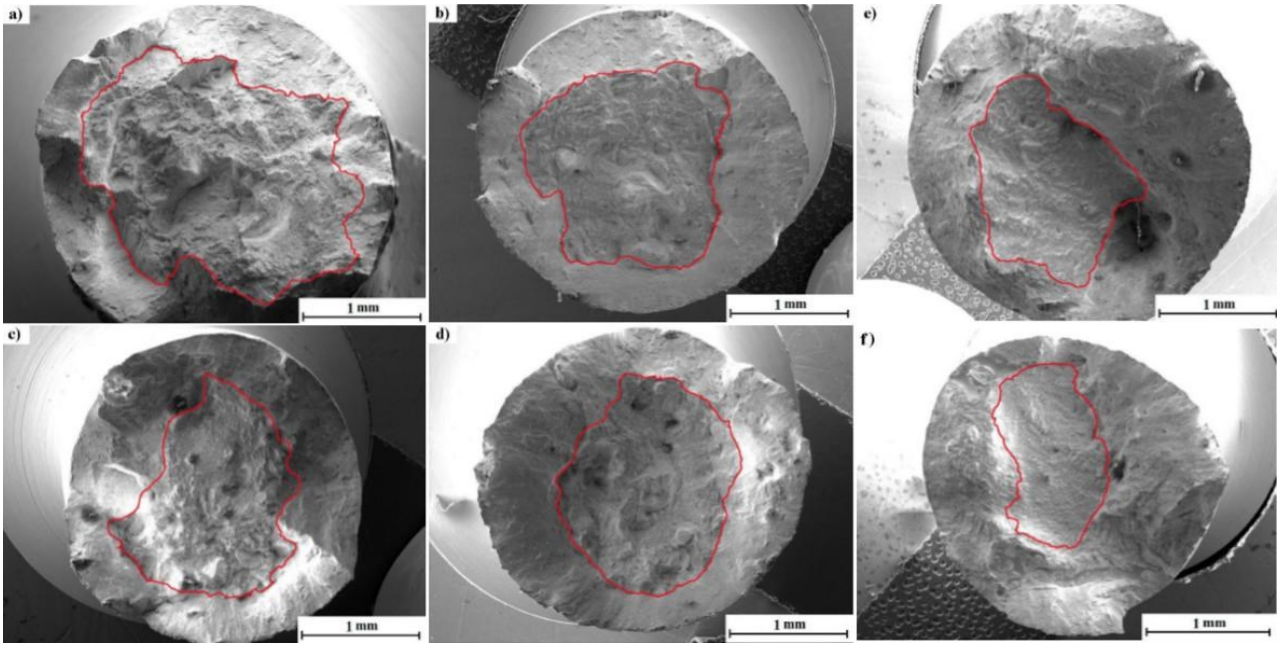

Figure 9 Fractography of the specimen LAR with mixed Ti6Al4V-*x*TA15 powders (a) *x*=50% (b) *x*=60 % (c) *x*=70% (d) *x*=80% (e) *x*=90% (f) *x*=100%

The macro-structure of the LRZ as shown in Figure 5, which were deposited with the mixed Ti6Al4V-*x*TA15 powders, shows that the width of primary β columnar decreases with the increase of

the mass fraction of TA15 in the mixed powders, leading to a higher grain boundary density. The enhancement of the grain boundary hinders the movement of dislocations. Therefore, the tensile strength is improved because of the barrier effect of grain boundaries on dislocations as the increase of the mass fraction of TA15 powders. Meanwhile, the primary α laths of LRZ were also refined with the increase of the mass fraction of TA15, lowering the deformation coordination ability within the retained β matrix and resulting in decreasing plasticity. It can be seen from Figure 8 that 20% Ti6Al4V powders mixed with 80% TA15 can significantly improve the plasticity of the LRZ but slightly reduce the tensile strength. As a whole, the mixed powders with TA15 powders mass fraction x=50%~80% (*i.e.*, corresponding Ti6Al4V powders' mass fraction is 20%~50%), are suitable for LAR of the TA15 forgings if considering the compatibility of the LRZ with the WSZ from the aspect of tensile properties.

Table 4 Areas encompassed by the solid red line shown in Figure 9.

TA15 ratio	50%	60%	70%	80%	90%	100%
Area /mm^2	3.42	2.89	2.61	2.14	1.58	0.98

Figure 9 shows the fractography of LRZ in the samples with a different mass fraction of TA15 for the mixed powders. The cup-cone fracture surface is exhibited as a central fibre zone and shear lip zone with a 45° of inclination from the tensile stress direction. The radiation zone is rarely revealed out, indicating that the specimen material has comparatively good plasticity. The areas of the central fibre zone which are encompassed by solid red line as shown in Figure 9, were calculated by Photoshop and Image-Pro Plus, aiming to characterize and quantify the plasticity of specimens. It can be seen from Table 4 that the calculated area of the central fibre zone decreases with the increase of the mass fraction of TA15, indicating the plasticity decreases accordingly as well. A small amount of incompletely-melted powders were observed on the fractural surface of some specimens and the crack propagation originated from the boundary of unmelted powders. However, as compared between with and without unmelted powders on the fracture surfaces, there is no significant difference in the tensile strength for specimens but of the same composition. It indicated that the tensile strength could be not so sensitive to incompletely-melted powders.

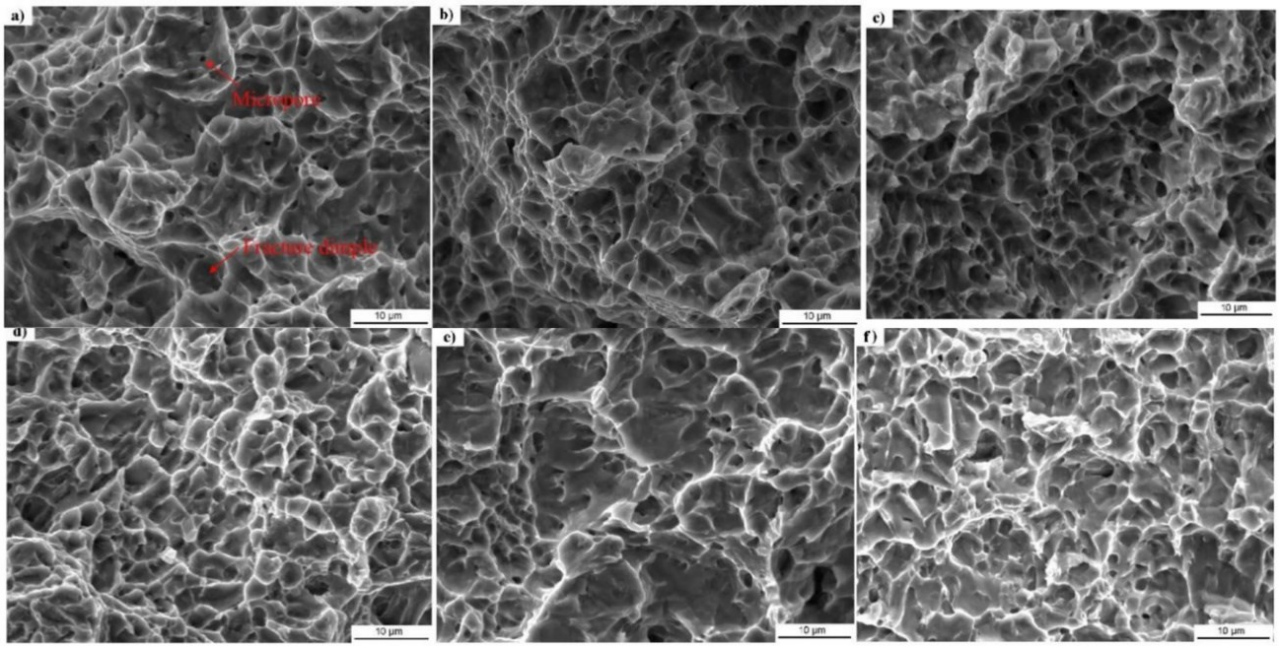

Figure 10 Micro fractography of the LAR samples with mixed Ti6Al4V-xTA15 powders (a) x=50% (b) x=60 % (c) x=70% (d) x=80% (e) x=90% (f) x=100%

Figure 10 shows the microfracture morphology of the central fibre zones. The fracture surfaces of the specimen LAR by mixed Ti6Al4V-*x*TA15 powders show dimples with web distribution. Through the aggregation of micropores at the bottom of dimples, ductile fracture of micropore aggregation type can be inferred as the fracture mechanism. The specimen LAR by Ti6Al4V-50%TA15 powders demonstrates the largest and deepest dimples, indicating the best plasticity. The dimples become smaller and shallower as the increase of mass fraction of TA15, indicating the decrease of material plasticity. These observations are consistent with the measured data of tensile strength and plasticity shown in Figure 8

3.3 Thermophysical and electrochemical properties

The difference in specific heat capacity and thermal expansion coefficient between the LRZ and WSZ may lead to residual stress during temperature variation. Cracks, delamination or other defects may occur at the interface and hence adversely affect the performance of LAR parts if the residual stress is large enough. Moreover, similar thermophysical property for the substrate and repair materials is beneficial to improve the dimensional accuracy and control thermal deformation at the interface. It is confirmed that the variation of the specific heat capacity of LRZ is less than 70 J/(kg·K) in the range of 303-873K and their average specific heat capacity as deposited with a different mass fraction of TA15 are listed in Table 5; the compatibility can be characterized as the ratios of the measured LRZ's specific heat capacity to that of the TA15 WSZ. With the increase of TA15 content, the average specific heat capacity of LRZ decreases gradually. The *x* range of 70%-100% is suitable in accordance with the compatibility calculation.

For most alloys, the heat capacity is the sum of the heat capacity for each component multiplied by its mass fraction ($C=X_1C_1+X_2C_2+...+X_nC_n$). As the temperature increases, the specific heat capacity of LRZ increases slowly and tends to be stable gradually. The specific heat capacity of the whole mixed powder system satisfies the linear superposition of the components-specific heat capacity. Therefore, the specific heat capacity of the whole system will decrease if the component with a lower specific heat capacity is increased. Table 6 shows the specific heat capacities of TA15 and Ti6Al4V alloys at different temperatures. The specific heat capacity of TA15 is generally lower than that of the Ti6Al4V. Therefore, the specific heat capacity of the mixed powders decreases gradually as the TA15's mass fraction increases.

Table 5 Average specific heat capacity(J/(kg·K)) at 303-873K and its compatibility

Material	TA15 WSZ	LRZ	Compatibility
50%	611	659	1.08
60%		646	1.06
70%		631	1.03
80%		636	1.04
90%		618	1.01
100%		607	0.99

Table 6 Parameters of heat capacity of Ti6Al4Vand TA15 (J/ (kg·K))

Material	373K	473K	573K	673K	773K
TA15	545	587	628	670	712
Ti6Al4V	624	653	674	691	703

Table 7 Average thermal expansion coefficient at temperature of 303-873K ($\alpha\times10^{-6}$/K)

Material	50%	60%	70%	80%	90%	100%
TA15 WSZ	10.4					
LRZ	10.6	10.8	10.8	10.9	11.0	10.9
Compatibility	1.02	1.04	1.04	1.05	1.06	1.05

We confirmed that little difference is revealed as the temperature rising for the thermal expansion coefficients of a certain *x*. Then the average thermal expansion coefficients for TA15 LRZ and WSZ are calculated in Table 7. The thermal expansion coefficients of LRZ are slightly higher than those of TA15 WSZ due to the higher content of phase and grain boundaries. Unlike the specific heat capacity, the microstructure of alloy has a critical influence on the thermal expansion coefficient [17,18]. With the increase of TA15's mass fraction, the width of the primary β columnar decreased slightly and interior α laths also were refined gradually; that is to say, more grain boundaries and phase interfaces exist in per unit volume. As we know, the atomic arrangement at the grain and phase boundaries is loose with a comparatively weak atomic bonding. Therefore, the atomic thermal vibration will be intensified, leading

to an increase in the thermal expansion coefficient. The *x* range of 50%-70% is more suitable as per the compatibility calculation shown in Table 7.

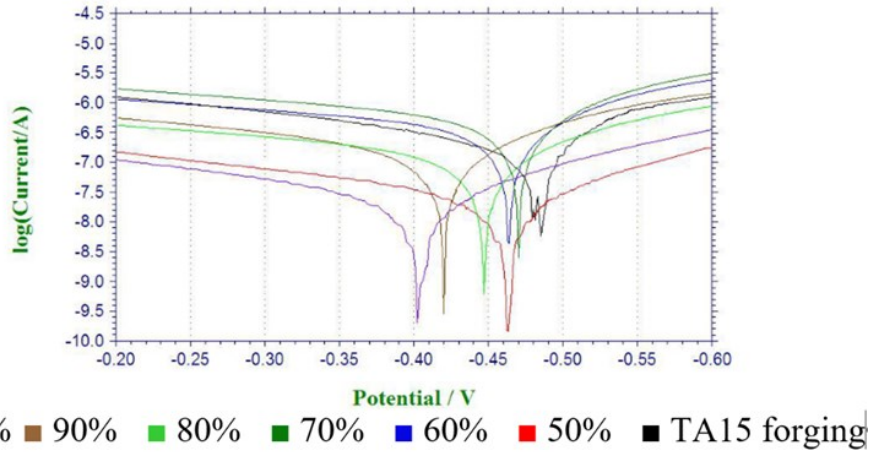

Figure 11 Tafel curves of the Ti6Al4V-*x*TA15 alloy in 3.5% NaCl

Electrochemical corrosion of specimens LARed by mixed Ti6Al4V-*x*TA15 powders with different TA15's mass fraction was measured. The Tafel curves are shown in Figure 11 and Table 8 shows the Tafel analysis results including self-corrosion potential E_{corr}, self-corrosion current density I_{corr} and polarization resistance Rp. It is found that with the increase of TA15's mass fraction, the self-corrosion potential shifts forward and the polarization resistance increases. Consequently, corrosion resistance of the LRZ is strengthened as the mass fraction of TA15 powder increases. Two possible reasons are concluded accordingly: (1) Mo is of the most positive electrode potential among the alloy components/elements which includes Ti, Al, V, Mo, and Zr as shown in Table 9 [19]; Mo content increases as TA15's mass fraction increases. According to the finding from OLIVEIRA et al. [20], the increase of Mo content in the titanium alloy can effectively improve stability of the passive film on the surface of titanium alloy in Cl-ion solution, resulting in increasing the corrosion resistance of the alloy. (2) The refined microstructure of LRZ (as shown in Figure 5 and Figure 6) also can improve the corrosion resistance. The content of the α phase in the LRZ decreases and the β phase increases with the increase of TA15's mass fraction. The content of Al in the α phase is slightly higher than that in the β phase, but Mo content in the β phase is higher than that in the α phase. Hence, the larger the volume fraction of the α phase is, the worse of corrosion resistance for the LRZ is.

To further visualize the segregation of elements in α and β phases, Figure 12 shows the elements distribution map of 100% TA15 LRZ. Al is an α stabilizer that is rich in the black band zone of the α laths in Figure 12 (a). While the locations with more Mo and V content are the white/grey areas shown in Figure 12 (a) and corresponds to the matrix. As β stable elements, Mo and V demonstrate a similar segregation rule as shown in Figure 12 (c) and (d). Zr is distributed uniformly in the whole region as a kind of neutral element shown in Figure 12(e).

Table 8 Analysis results of Tafel curves of the Ti6Al4V-*x*TA15 alloy in 3.5% NaCl

TA15 ratio	E_{corr} (V)	I_{corr} (A·cm $^{-2}$)	R_p (kΩ·cm $^{-2}$)
50%	-0.463	2.665×10^{-7}	61.56
60%	-0.464	5.962×10^{-7}	58.01
70%	-0.470	7.545×10^{-7}	65.94
80%	-0.447	3.252×10^{-8}	73.63
90%	-0.420	2.946×10^{-8}	79.59
100%	-0.402	2.615×10^{-8}	78.23
TA15 WSZ	-0.485	5.814×10^{-7}	31.33

Table 9 Standard electrode potential of various elements in titanium alloy [19]

	Ti	Al	V	Mo	Zr
E^{θ}/V	-0.386	-1.662	-1.175	-0.200	-1.553

Based on the compatibility calculation from mechanical, thermophysical and electrochemical properties, different mass fraction value of *x* suitable for specific property preference can be concluded and summarized as shown in Table 10. As a whole,

the Ti6Al4-70%TA15 is most suitable if an overall consideration on the compatibility of the LRZ with the WSZ in terms of the multiple properties, which is recommended as the raw material for LAR of TA15 forgings base material.

.

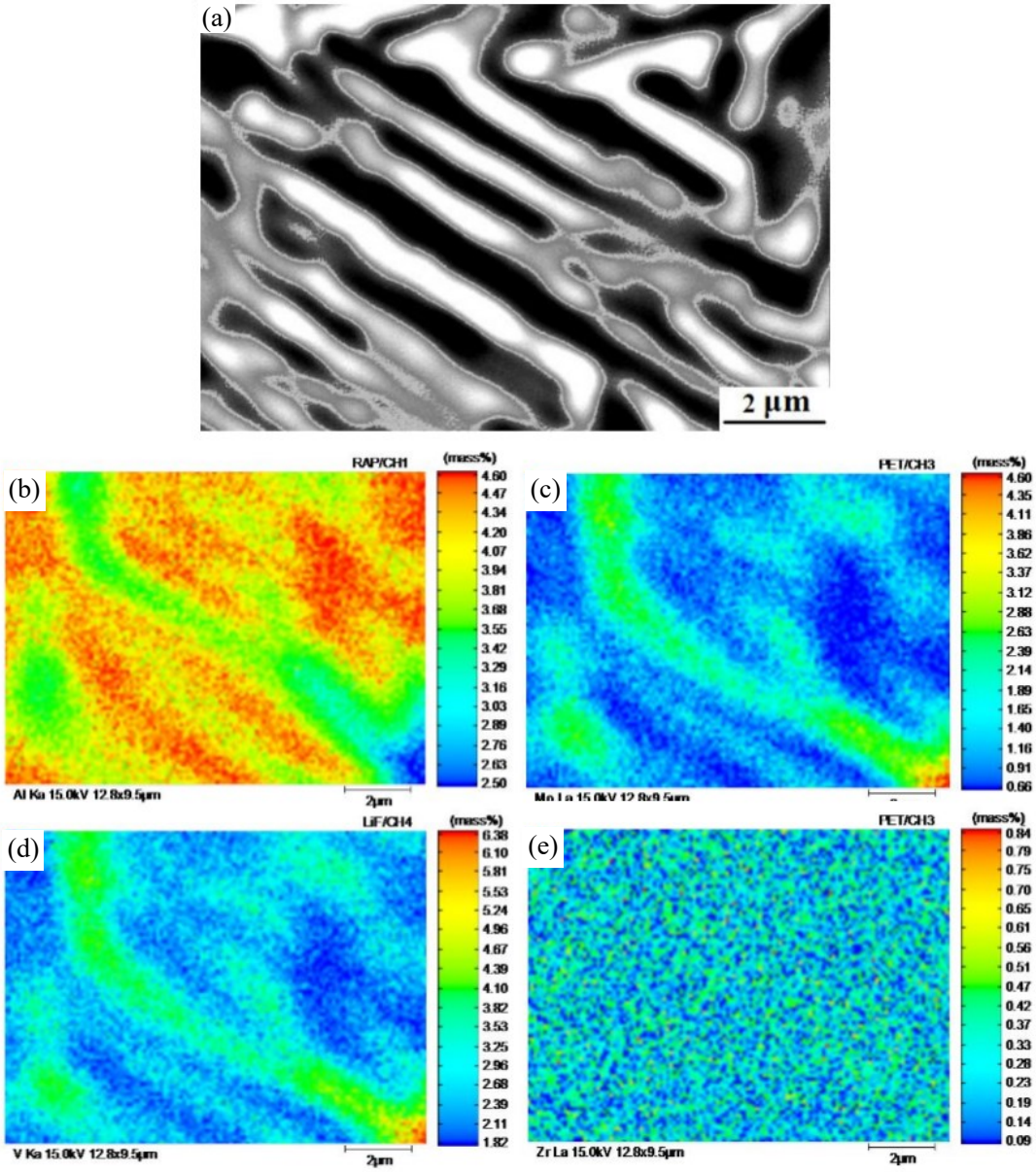

Figure 12 Distribution of elements in LRZ of 100%TA15 powder (a) original (b) Al (c) Mo (d) V (e) Zr

Table 10 The properties of different component of Ti6Al4-*x*TA15 and TA15 forging

	50%	60%	70%	80%	90%	100%
Tensile property	recommended					
Heat capacity				recommended		
Thermal expansion coefficient		recommended				
Corrosion resistance		recommended				

4 Conclusions

Laser additive repairing (LAR) is a new technology to directly repair the damaged zone for 3D parts. The compatibility and performance of

TA15 parts with mixed Ti6Al4V-*x*TA15 powders are studied based on a series of analyses on the microstructure and mechanical properties of the LAR parts. The main research conclusions are as follows:

(1) The primary β columnar were slenderer or refined with the increase of mass fraction *x* of TA15 considering the increment of quantity of high melting point elements Mo and Zr. The microstructure of Ti6Al4V-*x*TA15 specimens mainly consisted of basketweave-like primary α laths and retained the β phase. The α laths were refined with a higher TA15 mass fraction of Ti6Al4V-*x*TA15 powders because the content of the most effective β stabilizer Mo was increased that inhibited the growth of the α phase.

(2) The mechanical properties, including microhardness and tensile strength of LRZ part with mixed Ti6Al4V-*x*TA15 powders, were improved by 10%-27% and by 10%-17% increment as compared with those of the original TA15 forgings counterpart, respectively, with the increase of mass fraction *x* of TA15. The reduction of area ψ is sensitive to the powder ratio, leading to a maximal decrement for the Ti6Al4V-100%TA15 LRZ compared to the TA15 WSZ. Basically, the mechanical property is affected by the refinement of primary β columnar and primary α laths. As a whole, the mixed powders with TA15 powders' mass fraction x=50%~80% are suitable for LAR of the TA15 forgings in accordance with the compatibility of the LAR to the WSZ from the aspect of tensile properties.

(3) With the increase of TA15 content, the average specific heat capacity of LRZ decreases gradually. The *x* range of 70%-100% is suitable in accordance with the compatibility calculation. The thermal expansion coefficients for LRZ are slightly higher than TA15 WSZ due to the higher content of phase and grain boundaries. The atomic thermal vibration will be intensified, leading to an increase in the thermal expansion coefficient. The corrosion resistance of the LRZ is strengthened based on the increasing Mo content and the refined microstructure of LRZ, as the mass fraction of TA15 powder increases. The *x* range of 50%-70% is more suitable as per the compatibility calculations of the thermal expansion coefficients and corrosion resistance.

(4) Based on the compatibility calculation from mechanical, thermophysical and electrochemical properties, different mass fraction value of *x* suitable for specific property preference is concluded and summarized. As a whole, the Ti6Al4-70%TA15 is most suitable if an overall consideration on the compatibility of the LRZ with the WSZ in terms of the multiple properties, which is recommended as the raw material for LAR of TA15 forgings base material.

Contributors

The overarching research goals were developed by Jun Yu, Xin Lin and Weidong Huang. All experiment data were measured by Yepan Song under Xin Lin and Jun Yu's supervision. The initial draft of the manuscript was written by Jun Yu and Zhenjie Cao. Jun Yu, Zhenjie Cao, Quanren Zeng and Junjie Wang edited the draft of manuscript. All authors replied to reviewers' comments and revised the final version.

Conflict of interest

Jun Yu, Yepan Song, Xin Lin, Zhenjie Cao, Quanren zeng, Junjie Wang and Weidong Huang declare that they have no conflict of interest.

References

[1] CHAMANFAR A, PASANG T, VENTURA A, et al. Mechanical properties and microstructure of laser welded Ti–6Al–2Sn–4Zr–2Mo (Ti6242) titanium alloy [J]. Materials Science and Engineering: A, 2016, 663: 213-224. DOI: https://doi.org/10.1016/j.msea.2016.02.068

[2] GRIFFITH M L, SCHLIENGER M E, HARWELL L D, et al. Understanding thermal behaviour in the LENS process[J]. Materials & Design, 1999, 20(2-3): 107-113. DOI: https://doi.org/10.1016/S0261-3069(99)00016-3

[3] FATOBA O S, AKINLABI E T, MAKHATHA M E. Influence of rapid solidification on the thermophysical and fatigue properties of laser additive manufactured Ti-6Al-4V alloy[J]. Aluminum alloys, 2017, 181: 181-202. DOI: https://dx.doi.org/10.5772/intechopen.71697

[4] FACCHINI L, MAGALINI E, ROBOTTI P, et al. Ductility of a Ti‐6Al‐4V alloy produced by selective laser melting of pre-alloyed powders[J]. Rapid Prototyping Journal, 2010, 16: 450-459. ISBN: 978-1-78560-865-0

[5] FADIDA R, SHIRIZLY A, RITTEL D. Static and dynamic shear-compression response of additively manufactured Ti6Al4V specimens with embedded voids[J]. Mechanics of Materials, 2020, 147: 103413. DOI: https://doi.org/10.1016/j.mechmat.2020.103413

[6] ZHUANG Z, JING C, ZHANG Q, et al. Microstructure and mechanical properties of laser additive repaired Ti17 titanium alloy[J]. Transactions of Nonferrous Metals Society of China, 2017, 27(12): 2613-2621. DOI: https://doi.org/10.1016/S1003-6326(17)60289-9

[7] MARAZANI T, MADYIRA D M, AKINLABI E T.

Microhardness profiling of Ti-6Al-4V components repaired through multiple laser additive re-melt technique[J]. Procedia Manufacturing, 2019, 35: 897-902. DOI: https://doi.org/10.1016/j.promfg.2019.06.036

[8] ZHAO Z, CHEN J, TAN H, et al. Evolution of plastic deformation and its effect on mechanical properties of laser additive repaired Ti64ELI titanium alloy[J]. Optics & Laser Technology, 2017, 92: 36-43. DOI: https://doi.org/10.1016/j.optlastec.2016.12.038

[9] SUN Q, GUO K, WANG X, et al. Effect of scanning strategies on the microstructure and mechanical behaviour of 316L stainless steel fabricated by selective laser melting[J]. Materials Science and Engineering: A, 2020, 793: 139879. DOI: https://doi.org/10.1016/j.msea.2020.139879

[10] CHEN X, QIU C. In-situ development of a sandwich microstructure with enhanced ductility by laser reheating of a laser melted titanium alloy[J]. Scientific Reports, 2020, 10(1): 1-12. DOI: https://doi.org/10.1038/s41598-020-72627-x

[11] XIAOHONG Z, XIN L, JING C, et al. Effects of heat treatment on the microstructures and mechanical properties of TAl5 titanium alloys by laser solid forming[J]. Rare Metal Materials and Engineering, 2011, 40(1): 142-147. DOI:CNKI:SUN:COSE.0.2011-01-031

[12] LI J, LIN X, QIAN Y H, HUANG W D, Study on Microstructure and Property of Laser Solid Forming TC4 Titanium Alloy[J]. Chinese Journal of Lasers, 2014, 41: 1-5.(in Chinese) DOI:CNKI:SUN:JJZZ.0.2014-11-017.

[13] XU W, JUN M A, LUO Y, et al. Microstructure and high-temperature mechanical properties of laser beam welded TC4/TA15 dissimilar titanium alloy joints[J]. Transactions of Nonferrous Metals Society of China, 2020, 30(1): 160-170. DOI: https://doi.org/10.1016/S1003-6326(19)65188-5

[14] ZHANG Z, WANG Q, MO W, Metallurgy and heat treatment of titanium[M]. Beijing: Metallurgical Industry Press, 2009.(in Chinese) DOI: 10.11900/0412.1961.2018.00460

[15] ZHANG F, CHEN J, TAN H, et al. Chemical composition analysis for laser solid forming of titanium alloys from blended elemental powders[J]. Chinese Optics Letters, 2009, 7(3): 222-225. DOI: CNKI:SUN:JJZZ.0.2009-05-050.

[16] ZHANG Y, FENG S, DING C, et al. Investigation of the influences of heat treatment on the microstructures and thermal properties of Al-20Si alloy fabricated by powder extrusion[J]. Materials Characterization, 2020, 168: 110522. DOI: https://doi.org/10.1016/j.matchar.2020.110522

[17] GUAN S, WAN D, SOLBERG K, et al. Additive manufacturing of fine-grained and dislocation-populated CrMnFeCoNi high entropy alloy by laser engineered net shaping[J]. Materials Science and Engineering: A, 2019, 761: 138056. DOI: https://doi.org/10.1016/j.msea.2019.138056

[18] WANG J T, XIE L, WANG Z G, et al. Influence of laser shock peening on the coefficient of thermal expansion of Al (7075)-based hybrid composites[J]. Journal of Alloys and Compounds, 2020, 844: 156088. DOI: https://doi.org/10.1016/j.jallcom.2020.156088

[19] ZOSKI, C G. Handbook of electrochemistry[M]. USA: Elsevier, 2006. ISBN-13: 978-0-444-51958-0

[20] OLIVEIRA N T C, GUASTALDI A C. Electrochemical stability and corrosion resistance of Ti–Mo alloys for biomedical applications[J]. Acta Biomaterialia, 2009, 5(1): 399-405. DOI: https://doi.org/10.1016/j.actbio.2008.07.010

(Edited by HE Yun-bin)

中文导读

Ti6Al4V-xTA15 合金激光成形修复 TA15 锻件的相容性分析

摘要：本文提出了一种利用 Ti6Al4V-xTA15 混合粉末修复 TA15 锻件的简便可行方法。在 LAR 上应用不同质量分数的混合粉末，可以有效地保证修复后零件的性能和功能。本工作从显微硬度、拉伸性能、热容、热膨胀系数和耐腐蚀性能等方面全面研究了 Ti6Al4V-*x*TA15 粉末与 TA15 锻件的相容性。结果显示，随着 TA15 质量分数的增加，Ti6Al4V-xTA15 粉末细化了初生 α 板条，增加了次生 α 相的体积分数，导致其性能发生变化。综上所述，综合考虑激光修复区与锻造基板区域的相容性，Ti6Al4-70%TA15 (*x*=70%)混合粉末是最合适的候选材料，推荐该混合粉末作为 TA15 锻件激光成形修复的原料。

关键词：激光成形修复；TA15 合金；Ti6Al4V 合金；相容性